Acoustic and aerodynamic evaluation of POLIMI tandem propellers configurations within GARTEUR AG26

A. Zanotti, D. Granata, A. Savino, F. Caccia, L. Abergo, A. Guardone
Politecnico di Milano, Dipartimento di Scienze e Tecnologie Aerospaziali,
via La Masa 34, 20156, Milan, Italy
J.Yin, DLR - German Aerospace Center, Braunschweig, Germany
R. Wickersheim, M. Kessler, University of Stuttgart,
Institute of Aerodynamics and Gas Dynamics, Germany
A. Visingardi, M. Barbarino, CIRA - Italian Aerospace Research Centre,
Via Maiorise, 81043, Capua, Italy
A. Haas, H.-J. Kaltenbach, School of Engineering and Design,
Technical University of Munich, Germany
G. Reboul, DAAA, ONERA, Institut Polytechnique de Paris, 92320, Châtillon, France
G. Bernardini, C. Poggi, Roma Tre University,
Department of Civil, Computer Science and Aeronautical Technologies Engineering,
Via della Vasca Navale 79, 00146, Rome, Italy

ABSTRACT

The present work describes the activities performed in the GARTEUR Action Group HC/AG-26 to study the acoustic and aerodynamic characteristics of tandem propellers configurations, with a focus on the effects of mutual interactions between propellers typical of eVTOL aircraft. In particular, this paper describes comparisons between numerical activities and experimental results obtained over a dual propellers test case developed by Politecnico di Milano. The investigated configurations included both hover and airplane- mode flight condition with overlapping between propeller disks. Numerical results obtained by the partners simulations based on aerodynamic solvers characterised by different levels of fidelity from panel methods to CFD are compared to experimental results and discussed. Results comparison highlighted the capabilities and limits of the different numerical approaches to reproduce a quite challenging test case characterised by an high degree of unsteadiness due to propeller-propeller aerodynamic interaction and robust viscosity effects. Numerical predictions reproduce correctly the trends in aerodynamic parameters and changes in overall sound pressure level due to lateral shifts between propeller axis.

INTRODUCTION

Urban traffic of VTOL aircraft is expected to grow rapidly in next years due to the increase interest in the design of novel electric Vertical Take-Off and Landing (eVTOL) aircraft for Advanced Air Mobility (AAM), so that it will impact city planning criteria too. Investigation to understand noise pollution produced by a rotary-wing aircraft has used different ways of testing, both experimental, numerical and analytical. Full size tests are not always possible and could require a very high effort. Moreover, the use of scaled models in anechoic chambers or wind tunnels under monitored and controlled conditions can be considered a valuable tool also for validation of numerical simulation software.

To cite few works regarding investigation of multi-propeller acoustic signature, Thai et al. (Ref. [1]) investigated the interactions of small hovering rotors using both simulations and experimental analysis conducted in an anechoic chamber. In particular, a dual rotor interaction was analysed by reproducing a pair of co-rotating rotors and a pair of counter-rotating rotors positioned at different separation distance. Jia and Lee (Ref. [2]) investigate the acoustics of a quadrotor eVTOL using a high-fidelity simulation tool, concluding that no rotor-to-rotor interaction can be identified due to a vertical separation distance between the front and rear rotors and that the eVTOL fuselage does not have significant impact on acoustics, while both rotor aerodynamics and acoustics can be greatly influenced as the rotor size increases. Poggi et al. (Ref. [3]) present a numerical investigation of noise radiated by two side-by-side propellers showing that blade tip Mach number strongly affects the magnitude and directivity of the radiated noise, while

increasing the tip-clearance produces an increase of the spatial variability of the noise directivity for both co-rotating and counter-rotating configurations.

Recently, a great effort in the study of noise footprint related to multi-rotor configurations has been made by the activities conducted in the GARTEUR Action Group HC/AG-26, aimed at providing a comprehensive experimental database over different configurations of multi-propellers contributed by the partners. In this framework, experimental data were used for the validation of numerical solvers with different level of fidelity. Three main experimental activities were planned and performed in this framework. A first test case proposed by DLR (Ref. 4) consists of two small scale co-axial and tandem rotors configurations tested in an anechoic wind tunnel. The second test case is provided by CIRA/Cusano, consisting in a rig made by two-side-by-side propellers in hover (Ref. 5). The third test case that is object of the present paper is provided by Politecnico di Milano (POLIMI). Two propeller models reproducing typical eVTOL geometry were purposely designed and manufactured for the test campaigns that included both hover and cruise flight conditions of tandem configurations characterised by a certain degree of overlap between propellers disks. The present paper will focus on the numerical comparison activities with the experimental results obtained over this POLIMI dual propellers test configurations in two different test campaigns. The first campaign was performed in a wind tunnel and was aimed mainly to the characterisation of propeller-propeller aerodynamic interaction to in cruise flight conditions. The second test campaign was performed in an anechoic test chamber and was aimed to characterise both the aerodynamic and aeroacoustic behaviour of the two tandem propellers in hover flight conditions. For the numerical simulation of the various test cases, different approaches from each partner of the group were applied. Aerodynamic simulations necessary for the aeroacoustic evaluations were conducted with a different level of fidelity of the numerical methods, varying from panel-methods to hybrid uRANS/LES. In particular, numerical investigations were performed by applying either in-house-developed or commercial computational tools. The methodologies applied in the numerical simulations by the partners will be described and analyzed to point out their strengths and weaknesses by comparison of both the aerodynamic and acoustic evaluations with available test results for the different flight configurations.

EXPERIMENTAL SET UP

Propeller Model

Two propeller models were used for the test campaigns. The propeller hub was designed using hobby-grade components. In particular, a three-bladed hub equipped with left-handed VarioProp 12C blades was used, thus resulting in a propeller disk diameter D equal to 300 mm. A 65 mm diameter aluminium spinner was screwed on the propeller hub. An internal aluminium frame was designed to support the propeller driving system and a bi-axial strain gauge load cell. A FUTEK
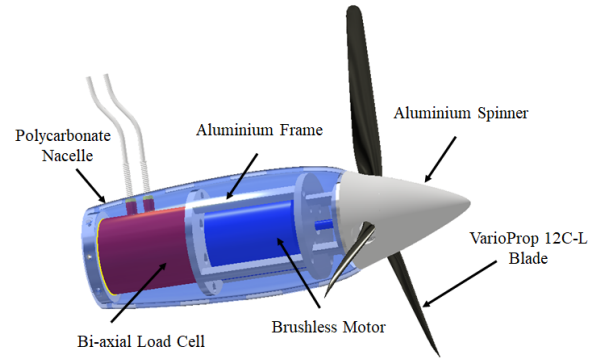

Figure 1. Layout of propeller model design (Ref. 6).

MBA500 strain gauge bi-axial load cell (50 lbs F.S.) mounted inside each nacelle was used to measure thrust and torque of each propeller. The load cell has a F.S. range of ±50 lbs for thrust and of ±50 lbs-in for torque, with ±0.25% Rated Out, non-linearity and ±0.05% Rated Out non-repeatability. The propeller was driven by a Scorpion brushless motor (5.3 kW continuous power) with shaft connected directly to propeller hub. The motor was powered by an external PWM-controlled electronic speed controller. A custom software developed in Labview was used to keep controlled both propellers at the desired rotational speed. A maximum fluctuation below 1% of the target rotational speed of the propellers was found during the tests. The azimuthal phase of the blade position of the two propellers was not synchronised. Indeed, the accurate control of propellers blade phase angles at the high RPM selected for the tests was not feasible due to hardware limitation of the hobby-grade external speed controller available for the tests. A polycarbonate nacelle with 270 mm length was manufactured using FDM technique and mounted on the internal metallic frame to shield both the motor and the load cell. More details on the propeller model design and manufacturing can be found in (Refs. 6, 7). Figure 1 shows the layout of the propeller model.

Cruise Test Campaign

A systematic series of wind tunnel tests were performed at the *S. De Ponte* wind tunnel of Politecnico di Milano (1 m × 1.5 m test section) over two propeller models in tandem configuration by changing their lateral separation distance (L_y) at fixed axial distance (L_x). Figure 2 shows the layout of the two propellers in tandem configuration including the definitions of the axial (L_x) and lateral (L_y) separation distance between propellers.

No acoustic measurements were performed in cruise flight conditions as the wind tunnel used is not anechoic. The propeller models were set up in the wind tunnel test section using metallic frames made by 30 mm × 30 mm squared section aluminium struts (see Fig. 3). A NACA 0025 airfoil shaped faring made by polystyrene was installed on the aluminium struts supporting the propellers. The two propellers
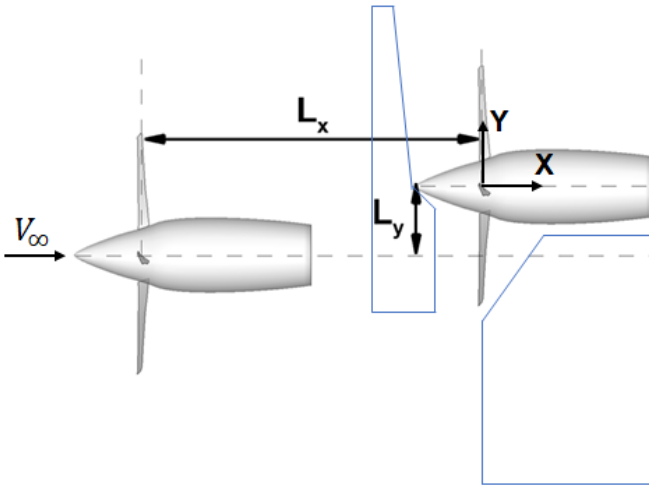
Figure 2. Layout of the tandem propellers in cruise flight condition configuration including separation distances and PIV planes dimensions.
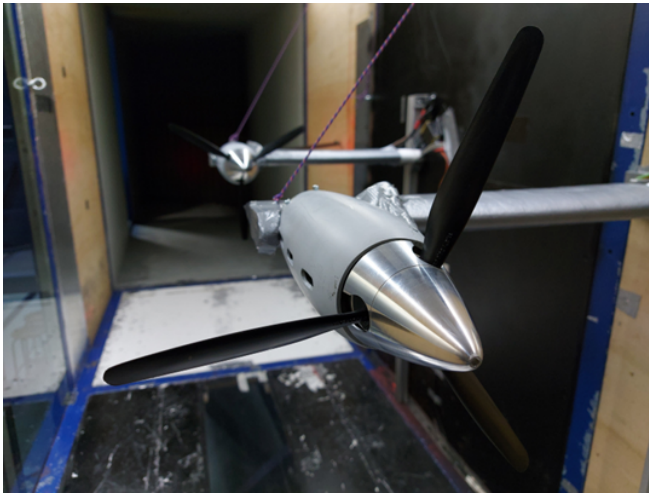

Figure 3. Set up of tandem propellers in cruise flight conditions at the *S. De Ponte* wind tunnel.

were mounted in tandem configuration with an axial distance (L_x) between the propellers disk equal to 5 rotor radii to reproduce a typical Vahana-like (Ref. 8) layout. The aluminium strut attached to one of the lateral walls of the wind tunnel test section, acting as a rail, enabled to modify the lateral separation distance between the models.

Wind tunnel tests included loads measurements (thrust and torque) to evaluate, particularly, the effects on rear propeller performance provided by aerodynamic interaction of front propeller slipstream. Moreover, the flow field around twin propellers configurations were investigated through stereo Particle Image Velocimetry (sPIV) technique. Two pairs of double-shutter cameras in stereoscopic mode were used to frame two different flow regions, respectively at inflow and in the near wake of the rear propeller (see PIV instrumentation set up in Fig. 4). The first camera pairs consisted of ILA.PIV.sCMOS CLHS cameras by Canon (Camera 1 and Camera 2 in Fig. 4) having a resolution of 2560 x 2160 pixels,
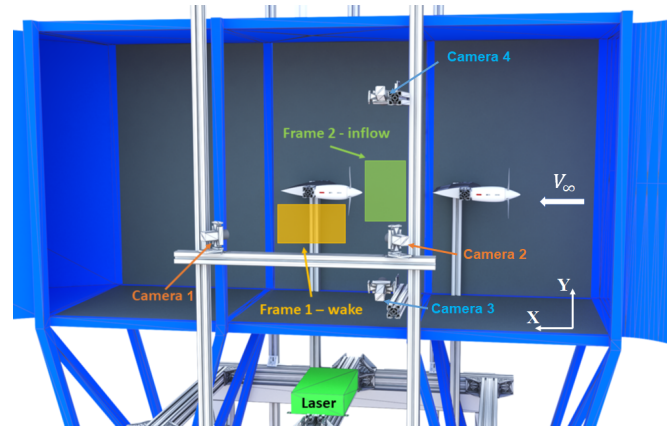

Figure 4. PIV set up for stereoscopic measurements on tandem propellers interaction at *S. De Ponte* wind tunnel.

16 bit dynamic range and were used to analyse the wake of the rear propeller. The second camera pairs consisted of Imperx ICL-B1921M CCD cameras (Camera 3 and Camera 4 in Fig. 4) with 12-bit 1952 × 1112 pixel array and were used to investigate the inflow of the rear propeller. The area of investigation for the inflow was 70 mm wide and 336 mm high, while the windows for the wake was 190 mm wide and 282 mm high. PIV surveys were performed both in free-run condition of the propellers and phase-locked with the azimuthal blade angle of the rear propeller.

The advance ratio range selected for the tests was aimed to evaluate interactional effects from a moderate to a fast cruise flight speed of eVTOLs aircraft flying in urban environment (Refs. 9, 10), while the propellers rotated at fixed 7050 RPM to reproduce a typical tip Mach number, i.e. $M_t = 0.325$, of full-scale eVTOL aircraft propellers in cruise flight condition (Refs. 8, 11). The blade pitch angle evaluated at 75%R of both propellers models was fixed to $26.5°$ for all the tests. Preliminary tests were performed over a single propeller (i.e. rear model) to characterise a reference aerodynamic performance for the evaluation of interactional effects by comparison with tandem propellers tests results. Stereo PIV surveys were performed for some selected test conditions, particularly focused on a typical target cruise flight velocity of an eVTOL aircraft in urban environment, i.e about 100 km per hour corresponding to an advance ratio J equal to 0.8. More details on the experimental set up can be found in (Ref. 6).

Hover Test Campaign

The experimental activity in hover flight conditions was performed at Politecnico di Milano in the $4m$ x $4m$ x $4m$ anechoic chamber of PoliMi Sound and Vibration Laboratory (PSVL). Tests were performed with the propellers rotating at fixed 9000 RPM. The blade pitch angle evaluated at 75%R of both propellers models was fixed to $15°$ for all the tests.

The propeller models were mounted on a metallic frame made by 30 mm × 30 mm squared section aluminium struts. The metallic frame was completely shielded with sound absorbing material. The aluminium strut used to support the pro-
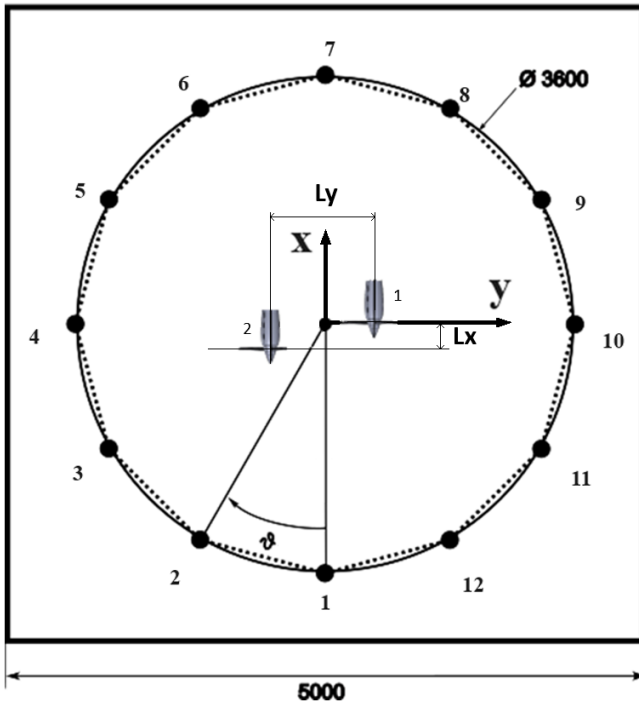
Figure 5. Scheme of propeller models in the anechoic test chamber and microphones positions highlighted as circular dots.

pellers, acting as a rail, enabled to manually modify the lateral separation distance between the models (L_y) in side-by-side configuration,i.e. with propellers disks lying on the same plane. Moreover, the metallic frame allowed to change also the longitudinal distance (L_x) between the propellers, thus enabling a tandem configuration with overlapping of the propellers disks. A sketch with the layout of the propellers in the anechoic test chamber highlighting the relative distances between the models and the microphones positions is shown in Fig. 5. Acoustic measurements were made by an array of twelve microphones positioned at 12 rotor radii (R) from the center of the test horizontal section aligned with the midspan of the propellers nacelle. Figure 5 shows as circular dots the microphones positions as well as the reference system for microphones azimuthal angle θ used in the results discussion. In the present work, the propeller depicted on the right of Fig. 5 is considered as the reference one. The layout of the tests set up is shown in Fig. 6.

The flow field around both the single and dual propeller configurations is investigated by means of stereo Particle Image Velocimetry (sPIV) technique with the aim of investigating blade vortex interactions and vortex-vortex interactions. Measurements were performed in a dedicated test campaign in a separate room with similar dimensions to avoid pollution of the anechoic test chamber. Two high-resolution 16 bit sC-MOS Cameras equipped with Canon© 28mm lens were arranged in angular Scheimpflug configuration, in order to make possible the reconstruction of the three-component displacement vector in the plane of the light sheet, as depicted in Fig. 7. During the experiment, the air flow was seeded with 1-2

Figure 6. Experimental set up in the PoliMI Sound and Vibration Laboratory (PSVL) anechoic chamber.

μm oil droplets generated by Laskin atomizer nozzles. Illumination was provided by a double-pulsed Nd:YAG laser emitting two pulses of 200mJ with 532 nm wavelength. In order to enlighten the area of interest on midspan plane between the two propellers, a 90° mirror was applied to the optics of the laser positioned on the floor. A general in-situ calibration procedure was conducted to obtain the mapping functions between the image planes and object planes for the sPIV measurements. The instantaneous velocity fields were obtained using a frame-to-frame multigrid cross-correlation technique using an interrogation window starting from 128 pixels × 128 pixels to 16 pixels × 16 pixels. An effective overlap of 50% of the interrogation windows was considered in PIV image pairs post-processing, thus resulting in a spatial resolution less than 2 mm between adjacent measurement points.

Test Conditions Selected for Numerical Comparison

A selected number of tested configurations in both hover (Hov) and cruise (CRF) conditions were considered for the comparison with numerical simulations from partners. Test conditions include both the single propeller (SP) configuration used as reference to evaluate the interactional effects provided by the front propeller, as well as the twin propellers (TP) with co-rotating sense of rotation (SoR). Table 1 presents the parameters of the tests conditions considered in the present paper results comparison analysis.

METHODOLOGIES USED BY PARTNERS FOR NUMERICAL SIMULATIONS

The numerical investigations were performed by each partner applying either in-house-developed or commercial computational tools. The aerodynamic simulations necessary for the aeroacoustic predictions were conducted using numerical methods with different range of fidelity, varying from panel methods to unsteady Reynold-Averaged Navier-Stokes (uRANS) simulations.
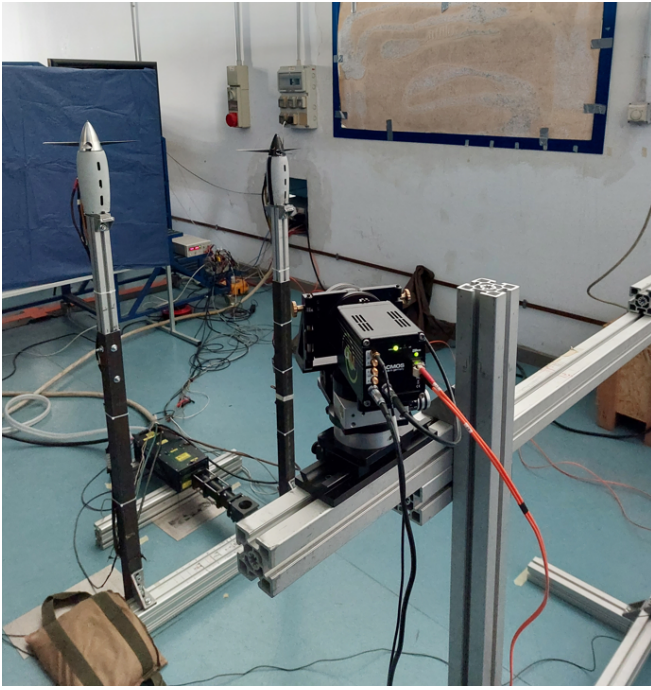
4

Figure 7. Stereo PIV experimental setup in hover.

Condition	RPM	θ at 75%R	SoR	L_x/R	L_y/R
CRF 1 (SP)	7050	26.5°	-	-	-
CRF 2 (TP)	7050	26.5°	Co-rot	5	0
CRF 3 (TP)	7050	26.5°	Co-rot	5	0.5
CRF 4 (TP)	7050	26.5°	Co-rot	5	1
Hov 1 (SP)	9000	15°	-	-	-
Hov 2 (TP)	9000	15°	Co-rot	0.5	2.5
Hov 3 (TP)	9000	15°	Co-rot	0.5	2
Hov 4 (TP)	9000	15°	Co-rot	0.5	1.5

Table 1. Test parameters of the investigated configurations.

Politecnico di Milano (POLIMI)

The test cases in cruise were simulated with both a mid-fidelity and a high-fidelity aerodynamics solver, respectively DUST and SU2. For the hover conditions, DUST was used to compute the aerodynamic solutions for both single and tandem configurations, while SU2 was used for the single propeller configuration only. DUST is an open-source software developed by POLIMI to simulate the interactional aerodynamics of unconventional rotorcraft configurations. The code, released as free software under the open-source MIT license, relies on an integral boundary element formulation of the aerodynamic problem and on a vortex particle model of the wakes (Ref. 12). In particular, non-linear vortex lattice (NLVL) elements were used in DUST to model the blades, while surface panels were used to model the spinner-nacelle system. The NLVL chord-wise discretization is built using 5 collocation points with a spanwise discretization of 50 elements for each propeller blade. DUST simulations span 10 rotor revolutions with a time discretization equivalent to 5° of blade azimuthal angle. SU2 is an open-source toolkit dis-

tributed by the SU2 Foundation (Ref. 13), freely available and licensed under the GNU Lesser General Public License. It uses the finite volume approach to solve partial differential equations (PDE) on unstructured meshes. It solves the uRANS equations to analyze typical aeronautical problems that involve turbulent flows in the compressible regime. In this work, a steady RANS simulation in a rotating reference frame (RRF) approach (Ref. 14) is used for the single propeller configuration. Fully unsteady simulations applying a sliding mesh technique (SM) (Refs. 15,16) are used to solve the aerodynamic field for the tandem configurations. This approach is necessary when dealing with complex scenarios, such as non-axial flight conditions and multiple propellers with arbitrarily relative positions. Among the several options offered within SU2, the central Jameson-Schimdt-Turkel (JST) scheme for convective fluxes discretization has been applied in all the computations (Ref. 17). Turbulence has been modeled with the Spalart-Allmaras (SA) model (Ref. 18). Concerning the steady simulations, the standard SA is modified by the algebraic BCM transition model from (Ref. 19). In the case of unsteady simulations, a second-order dual time-stepping method is used, and the time-step is fixed to achieve 1° of blade azimuthal angle. To ensure the accuracy of the reference data, the independence of the solution on spatial discretization is investigated by comparing three different grid resolutions. All grids are characterized by a y^+ value of 1 at the wall to operate within the hypotheses of the turbulence model. The first grid, referred to as SU2-coarse, has fewer surface points and a coarser wake discretization compared to the others. The grids for single and tandem propellers are characterized by a y^+ value of 1 at the wall to operate within the hypotheses of the turbulence model and by a number of cells respectively of 56.6 and 72.2 millions in the whole domain.

Aerodynamic results obtained with both solvers are not trimmed. The aeroacoustic signature is computed by solving Ffowcs-Williams and Hawkings (FWH) equations (Ref. 20). The surface pressure field on the propeller computed with the two solvers is provided as input to the same acoustic module (Ref. 21).

DLR

The free-wake panel method UPM (Refs. 22,23) is based on a velocity-based, indirect potential formulation using a combination of source and vortex distribution on the solid surfaces and vortex panels in the wake. A short zero-thickness elongation of the trailing edge along its bisector, called Kutta panel, ensures the flow tangency condition at the trailing edge and defines the total strength of the circulation at the blade section. An iterative pressure Kutta condition is implemented to subsequently ensure pressure equality at the trailing edge. This method is proved to be computationally efficient and robust with respect to the size of the chosen time step and the number of panels on the blade. The pressure on the blade surface is calculated from the unsteady Bernoulli equation. Compressibility effect of the flow are considered by applying the Prandtl-Glauert correction. The free wake is repre-

sented in the form of connected vortex filaments and is released from the downstream edge of the Kutta panel. The wake can also be represented in the form of vortex particles as UPM is linked to a particle solver. The blade vortex interaction (BVI) is captured thanks to the free wake model used in UPM. Although UPM is a potential code, the displacement effect of the boundary layer on lifting surfaces can be modelled through a viscous-inviscid coupling scheme. The boundary layer parameters, especially the displacement thickness was derived using an approximate boundary layer (BL) analysis. In current paper a viscous-inviscid coupling is included. In addition, a Rankine vortex model with a linear core radius dissipation model was applied for both full and tip vortex.

The Aeroacoustic Prediction System based on an Integral Method, APSIM (Ref. 24) is designed to calculate wave propagation over large distances in uniform flows. The methodology is based on Ffowcs-Williams and Hawkings formulation (Ref. 20) and only linear sound propagation is considered. In general, the aeroacoustic computation into the far field is split into two steps for current applications: In a first step the pressure data on the rotor is computed by aerodynamic codes and provided to APSIM; in a second step the sound propagation into the far field is calculated with APSIM. Validations of UPM, and APSIM were intensively conducted during various projects.

For the numerical simulation applied in current paper, each blade was discretized by 57 chordwise × 30 spanwise panels and no nacelle and spinner were simulated. The computations started with a step size of 5° azimuth and this was reduced to 2° after initial wakes pass away from both rotors. An overestimation of the thrust in isolated rotor cases was obtained when applying the nominal blade pitch $\theta_0 = 26.5°$ in the simulation for the forward flight. A trim procedure was adopted consisting in evaluating the blade pitch providing the experimental thrust in isolated rotor conditions. The new blade pitch was found to be equal to $\theta_0 = 23.74°$, thus with a reduction in pitch of 2.76°. This value was kept as constant for all the other runs in axial flight. Similarly, the same procedure was adopted for the hover flight: the blade pitch producing the nominal thrust was found to be equal to $\theta_0 = 14.3°$ instead of the nominal value of $\theta_0 = 15°$, with reduction in pitch of 0.7°. This new pitch angle was kept as constant for all the other runs in hover flight.

ONERA

The aerodynamic simulations performed by ONERA are realized with the PUMA code (Ref. 25) for the cruise test cases only. PUMA (potential unsteady methods for aerodynamics) is an unsteady lifting line / free-wake solver developed at ONERA since 2013. It is built on a coupling between an aerodynamic module and a kinematic module. The aerodynamic module relies on a lifting line method with a free-wake model using the Mudry theory (Ref. 26), which describes the unsteady evolution of a wake modeled by a potential discontinuity surface. The lifting line method relies on two-dimensional

airfoils characteristics through lookup tables computed preliminary by CFD with the ONERA elsA V4.2.01 Airbus-Safran-ONERA property code (Ref. 27). Some blade sweep correction and dynamic stall models are added. Concerning the kinematic module, it is based on a rigid multi-body system approach using a tree-like structure with links and articulations. It enables any arbitrary motion between the different elements. In order to speed up the computation the code has been parallelized using OpenMP and the Multilevel Fast Multipole Method has been implemented. Regarding the numerical parameters used for the computations, they are based on previous experience. The lifting line is divided in 30 radial stations using a square root distribution. A time step of 2° was used over 8 rotor revolutions over which the last 4 are used for post-processing. The computations do not account for the rotor hub or other test rig components and the propellers are not trimmed to eventually match the experimentally measured thrust. The unsteady spanwise distribution of loads obtained with PUMA are used as input for the KIM code (Refs. 28,29) to determine the noise emission of the rotor thanks to a Ffowcs-Williams and Hawkings formulation implemented in a non-compact advanced time approach. Since only sectional forces are available and in order not to consider noise sources compact in the chord direction, the surface pressure is reconstructed over the entire blade thanks to interpolation based on the pressure distributions computed and stored during the airfoil polar computations.

University of Stuttgart (IAG)

The numerical tool chain at the Institute of Aerodynamics and Gas Dynamics (IAG) at the University of Stuttgart employs the CFD solver FLOWer (Refs. 30–32) coupled to the Ffowcs-Williams and Hawkings in-house Code ACCO (Ref. 33). FLOWer solves the uRANS equations on structured grids by applying the Menter-SST turbulence model for closure (Ref. 34). In addition, a second-order dual-time stepping scheme is utilized for temporal discretization, with a time step of 0.5°, and a second-order James-Schmidt-Turkel scheme for spatial discretization. To accurately resolve propeller tip vortices, a 6th-order weighted essentially non-oscillatory (WENO) scheme is applied in the background mesh (Ref. 35). The Chimera technique facilitates relative motion among structural elements by employing separate meshes for each propeller blade and spinner. These meshes are situated in a background mesh containing hanging grid nodes to reduce computational expense. The boundary layers of the structures are sufficiently resolved to meet the criteria $y^+ < 1$ with a cell growth rate of 1.2 extruded to a resolution of 10% of the propeller chord length. The total cell count, encompassing all structure meshes and the background mesh, amounts to 83 million cells, with each propeller blade mesh contributing approximately 1 million cells, the spinner 2.5 million cells, and the background mesh 72 million cells. For the acoustic extrapolation to the far-field observer positions, the surfaces of the propeller blades are utilized as acoustic integration surface for the FWH equation (Ref. 20). In this

study considering only cruise conditions, two full propeller revolutions are employed for the acoustic evaluation, considering mean flow effects in the FWH approach.

CIRA

The CIRA aerodynamic simulations were carried out by using the medium-fidelity code RAMSYS (Ref. 36), which is an unsteady, inviscid and incompressible free-wake vortex lattice boundary element methodology (BEM) solver for multi-rotor, multi-body configurations developed at CIRA. It is based on Morino's boundary integral formulation (Ref. 37), for the solution of Laplace's equation for the velocity potential. The surface pressure distributions are evaluated by applying the unsteady version of Bernoulli equation, which is then integrated to provide the forces and moments on the configuration and the surrounding obstacles. A computational acceleration is obtained by applying the module for symmetrical flows and geometries implemented in the solver and the parallel execution via the OpenMP API.

The ACO-FWH solver is used for computing the acoustic free-field generated by the rotor blades. It is based on the FWH formulation (Ref. 20), as described in (Refs. 38–40). The advanced-time formulation of Farassat 1A is employed, and the linear terms (the so-called thickness and loading noise contributions) are computed through integrals on the moving blades' surface (impermeable/rigid surface formulation). The computational acceleration is obtained by a parallel execution via the MPI API. The simulation of the aeroacoustic free-field was carried out by using the aerodynamic database evaluated by RAMSYS, and consisting of the rotor blade pressure distributions.

Each blade was discretized by 60 chordwise $\times$ 21 spanwise panels, while 1886 panels were used to discretize each nacelle and spinner geometries. The wake geometry was modelled by six spirals and six propeller revolutions in axial flight, and by ten spirals and ten propeller revolutions in hover flight. A time step corresponding to an azimuth step of $2°$ was used to discretize each wake spiral. Initial simulations were carried out in axial flight, at the advance ratio J=0.8, at the nominal blade pitch $\theta_0 = 26.5°$. Unexpectedly, the resulting thrust turned out to be extremely overestimated (about 40%) with respect to the experimental value. For this reason, a trim procedure was adopted consisting in evaluating the blade pitch providing the experimental thrust. The new blade pitch was found to be equal to $\theta_0 = 22.56°$, thus with a reduction in pitch of $3.94°$. This value was kept as constant for all the other runs in axial flight. Similarly, the same procedure was adopted for the hover flight: the blade pitch producing the nominal thrust was found to be equal to $\theta_0 = 13.67°$ instead of the nominal value of $\theta_0 = 15°$, with reduction in pitch of $1.33°$. This new pitch angle was kept as constant for all the other runs in hover flight. In order to enable a rapid adjustment of the blade pitch, the blades were detached from the spinner, which was kept as fixed during the propellers' revolutions.

TU Munich (TUM), Flow control and aeroacoustic group

The commercial CFD software Ansys Fluent 23.R1 is used to carry out transient simulation for tandem configurations using the sliding mesh technique with two rotating domains embedded in a non-rotating outer domain. A structured multi-block mesh created with ICEM-CFD with about 20 millions hexaedral cells is employed. The wall-normal resolution was set to satisfy $y^+ < 1$. The sensitivity with respect to grid resolution along the blade surfaces and in the wake region between the two propellers has been checked. Here, results for the $k - \omega$-SST model and the hybrid RANS-LES approach denoted SBES are reported. Due to the low chord-based Reynolds number additional simulation were carried out with the $\gamma - Re_\theta$ transition model, yielding a laminar boundary layer on the pressure side and substantial regions with laminar separation on the suction side followed by turbulent reattachment. The use of the transition model yielded slightly lower values of thrust and torque in better agreement with measurements and had little effect on the predicted noise. The pressure based solver with the SIMPLE procedure was used for air modeled as ideal gas, employing an implicit second order scheme in time and 2nd order upwind differences for spatial derivatives for the uRANS simulation. For the hybrid RANS/LES bounded second order central differences were used, yielding much lower dissipation of the tip vortices. Time advancement proceeded with 360 time steps per revolution using 5-10 inner iterations. At the end surfaces of the cylindrical outer domain with a diameter of 10 blade radii a velocity inlet and a pressure outlet were specified. The radial far field boundary was set as pressure outlet as well, allowing backflow with the direction inferred from neighbouring cells in order to allow for radial entrainment. Acoustic prediction were obtained from the blade surface pressure with the time-domain FWH code "SPySI" developed at FAU Erlangen (Ref. 41).

Roma Tre University (ROM3)

The aerodynamic and aeroacoustic analyses rely on tools developed by the Roma Tre University unit in the last twenty years and widely validated in the past in helicopter and tiltrotor configurations (Refs. 42, 43). The aerodynamic module is based on the boundary integral formulation for the velocity potential presented in (Ref. 44), suited for helicopter configurations where BVI occurs. This formulation is fully 3D, can be applied to bodies with arbitrary shape and motion, and allows the calculation of both wake distortion and blade pressure field. It assumes the potential field to be divided into an incident field, generated by doublets over the wake portion not in contact with the trailing edge (far wake), and a scattered field, generated by sources and doublets over the body and doublets over the wake portion very close to the trailing edge (near wake). This procedure allows one to overcome the instabilities arising when the wake comes too close to or impinges on the body. Recalling the equivalence between the surface distribution of doublets and vortices, the contribution of the

wake portion experiencing BVI (far wake) is expressed in thick vortex (i.e., Rankine vortices) distributions. The wake's shape can be either assigned (prescribed-wake analysis) or obtained as a part of the solution (free-wake analysis) by a time-marching integration scheme in which the wake is moved according to the velocity field computed from the potential solution. Once the potential field is known, the Bernoulli theorem yields the pressure distribution on the body that, in turn, is used both to determine the aerodynamic loads and as an input to the aeroacoustic solver to predict the radiated noise. The aeroacoustic analysis is performed by a prediction tool based on the FWH equation (Ref. 20). The solution of the FWH equation is achieved through the boundary integral representation known as the Farassat Formulation 1A (Ref. 45). The numerical model of the propeller in the present activity was built using a discretization of 50 elements in both chordwise and spanwise directions for each propeller blade. Simulations span 6 rotor revolutions with a time discretization equivalent to 3° of blade azimuthal angle.

RESULTS AND DISCUSSION

Cruise Flight Conditions

Aerodynamic Performance

A first validation of the numerical solvers is given by comparing the averaged thrust C_T and power coefficients C_T of the single propeller (CRF 1) calculated with the different numerical approaches with respect to experimental data, see Tab. 2. In the experiments, the load cell measures the sum of axial forces on the 3 blades and the spinner, while for the numerical results the forces acting on the blades are reported. High-fidelity CFD results suggest that the drag of the spinner reduces the thrust by about 1%.

	C_T	C_P
Experimental	0.1001	0.1122
POLIMI - DUST	0.1004	0.099
POLIMI - SU2 (RANS RRF)	0.1021	0.1145
CIRA (trimmed)	0.1002	0.0154
DLR (trimmed)	0.9941	0.0149
ONERA	0.1133	0.1251
IAG (uRANS)	0.1065	0.1150
TUM (uRANS)	0.1117	0.1220
ROM3	0.0995	0.0150

Table 2. Thrust and Power coefficients evaluated for the single propeller in cruise flight condition CRF 1 (SP) by the different computational methods.

A good agreement was found for C_T and C_P evaluated by high-fidelity CFD approaches, i.e POLIMI-SU2, IAG, showing differences with respect to experimental value respectively below 6% and 3%. Discrepancies higher than 10% were found for the uRANS approach used by TUM. Possible reasons for the deviations between CFD predictions include differences in turbulence models, domain size and farfield

boundary condition, discretisation scheme and grid resolution. Mid-fidelity approach used by POLIMI-DUST taking into account viscous corrections enabled to obtain a quite good accuracy for the calculation of both thrust and torque of the single propeller in cruise comparable to high-fidelity CFD. The mid-fidelity approach used by ONERA reveals slightly higher discrepancies considering the thrust coefficient with respect to DUST solution, while almost the same discrepancy is found for the power coefficient. In ONERA case, viscous effects are taken into account via the computation of airfoil lookup tables thanks to RANS simulations. On the other hand, DLR and CIRA results show solutions trimmed on C_T value but do not provide similar accuracy on C_P evaluation that is largely underestimated due to the fact that they both consider a pure potential solution. For the same reason also ROM3 approach largely underestimates the propeller torque but without any trimming procedure is capable to capture with high degree of accuracy the experimental thrust coefficient.

Simulations results for the tandem configurations (CRF 2-4) obtained by the different numerical approaches are compared to experimental data in Fig. 8, showing the ratio of the thrust and power coefficients evaluated for the rear propeller with respect to single propeller (CRF 1). This representation enables to highlight the capabilities of the solvers to capture the aerodynamic performance losses of the rear propeller due to the interaction of the front propeller slipstream.

For the co-axial configuration ($L_y/R = 0$) characterised by the highest degree of interactional effects, experimental data show performance losses for the rear propeller in the order of 30% and 20% respectively for C_T and C_P. An overestimation of the thrust loss was found by all numerical solutions. A better agreement with experiments was found for the mid-fidelity approaches used by POLIMI-DUST, ROM3 and CIRA, DLR solutions with the latter two trimmed on single propeller C_T value. In this case, uRANS approaches shows higher losses with respect to mid-fidelity solutions, despite IAG approach showing a similar results to DLR. An overestimation of the performance losses was found also for C_P values, even if, as expected, the high-fidelity approach for this parameter is more accurate with respect to mid-fidelity solutions. Nevertheless, pure potential solutions show good capabilities to capture the performance losses. For the tandem configurations with partial propeller disks overlap, performance losses decrease and the accuracy of the numerical solutions increase for both C_T and C_P. Indeed, in these cases the discrepancies with respect to experiments obtained with mid-fidelity and high-fidelity solutions for the rear propeller C_T becomes below 10% and 5% respectively for the $L_y/R = 0.5$ and $L_y/R = 1$ configurations.

Aerodynamic solutions analysis is completed by the comparison of the averaged flow fields evaluated by the different numerical solvers with respect to PIV data. In particular, Figs. 9-11 show the comparison of the contours of the averaged axial velocity component (*u*) for the tandem configurations CRF 2-4 around rear propeller region.

For the co-axial configuration ($L_y/R = 0$), the PIV flow field shown in Fig. 9(a) highlights the remarkable influence of
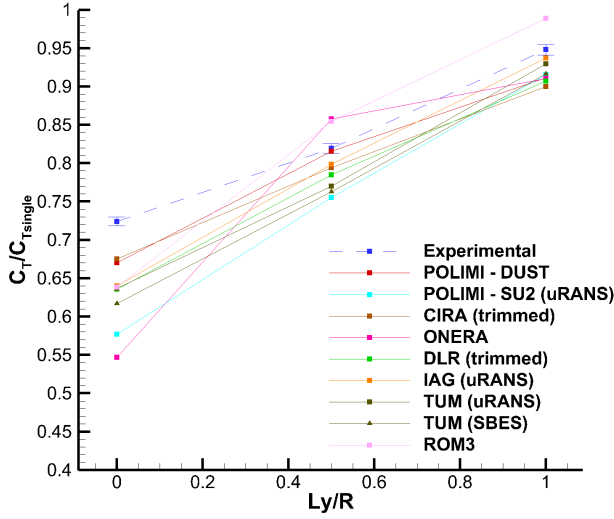
(a)
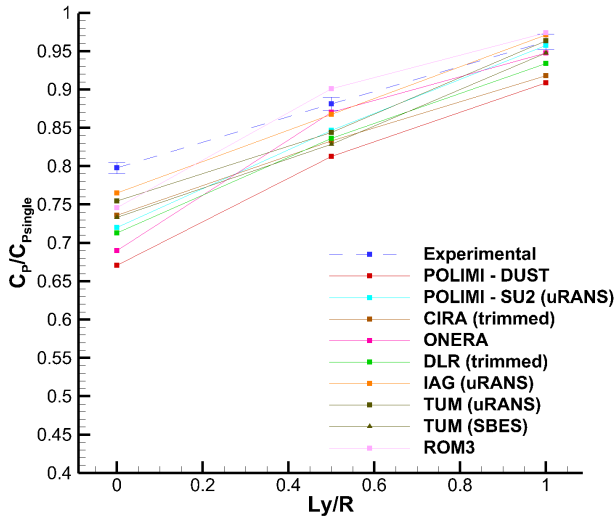
(b)

Figure 8. Thrust and Power coefficients evaluated for the rear propeller in tandem CRF 2-4 (TP) with respect to single propeller CRF 1 (SP) in cruise flight condition by the different computational methods.

the front propeller slipstream on the rear propeller disk inflow. A significant acceleration of the rear propeller outer wake region is observed from axial velocity component representation. Numerical simulations results show a quite good agreement with experiments for both mid- and high-fidelity approaches, capturing with good accuracy the topology of the PIV flow field and a symmetric flow pattern. In particular, numerical simulations shows a slightly higher acceleration in the rear propeller slipstream, while a better agreement with experiments is found for the trimmed solution obtained by DLR. Moreover, the main difference between high- and mid-fidelity

solutions is that uRANS approaches have the capability to reproduce correctly the wake of the rear propeller nacelle. No noticeable differences are found between the mean flow field representations obtained by TUM using either uRANS or SBES as model. Individual tip vortices (not shown) are much better represented by the SBES model for which the numerical dissipation was reduced by the use of bounded central differences. This feature is apparent for all the tandem propellers test cases considered in this analysis.

A more evident effect of the aerodynamic interaction between the propellers is visible when increasing the separation distance between them to $L_y/R = 0.5$. In this configuration an asymmetric behaviour of the rear propeller inflow is observed in the rear propeller wake (see Fig. 11(a)). In particular, the upper region of the front propeller slipstream is forced to overcome the rear propeller nacelle with an upward deviation. This produces an accelerated flow region due to the spinner curvature over the rear nacelle that is quite well captured by numerical simulations. The observation of PIV measurements highlights also that the lower inner portion of the front propeller wake is interacting with the lower region of the rear propeller wake. The outcome of the interaction is a non-uniform accelerated flow region that is expanding as long as the wake progresses. Once again, the numerical solutions capture this interactional feature, showing an accelerated region in the lower portion of the rear propeller blade. A flow field representation from SU2 is not available for the present test case as well as the aeroacoustic solution.

Flow field analysis for the configuration with $L_y/R = 1$ clearly shows that the lower portion of the rear propeller disk is fully immersed in the front propeller wake, showing major effects with a strongly accelerated flow region in this area (see PIV results in Fig. 11(a)). Numerical simulations are in quite good agreement with experimental survey particularly in the lower portion of the rear propeller wake that is strongly affected by the acceleration imposed by the front propeller slipstream.

Aeroacoustics

Aeroacoustics evaluations were compared in terms of the overall SPL in polar diagrams. In particular, for the single propeller configuration in cruise, virtual microphones positions were defined in the X-Y midspan plane on points equally distributed from $\theta = 0°$ (upwind) to $\theta = 360°$ (downwind) with $10°$ step at a Euclidean distance of 5 blade radii (R) from the center of rotation of the propeller (see Fig. 12(a)).

For the tandem propellers configurations the overall SPL is compared on X-Y midspan plane on two sets of points. The first set of 10 points is centered in the center of rotation of the front propeller disk and is placed at 5 blade radii (R) distance covering an angular range from $\theta = -90°$ to $\theta = 90°$ in front of the rotor (see Fig. 12(b)). The second set of 10 points is centered in the center of rotation of the rear propeller disk and is placed downwind at 5 blade radii distance covering an angular range from $\theta = 90°$ to $\theta = 270°$, see Fig. 12(b).

For the single propeller configuration in cruise (CRF1) the polar plot of the overall SPL computed by simulations shows a

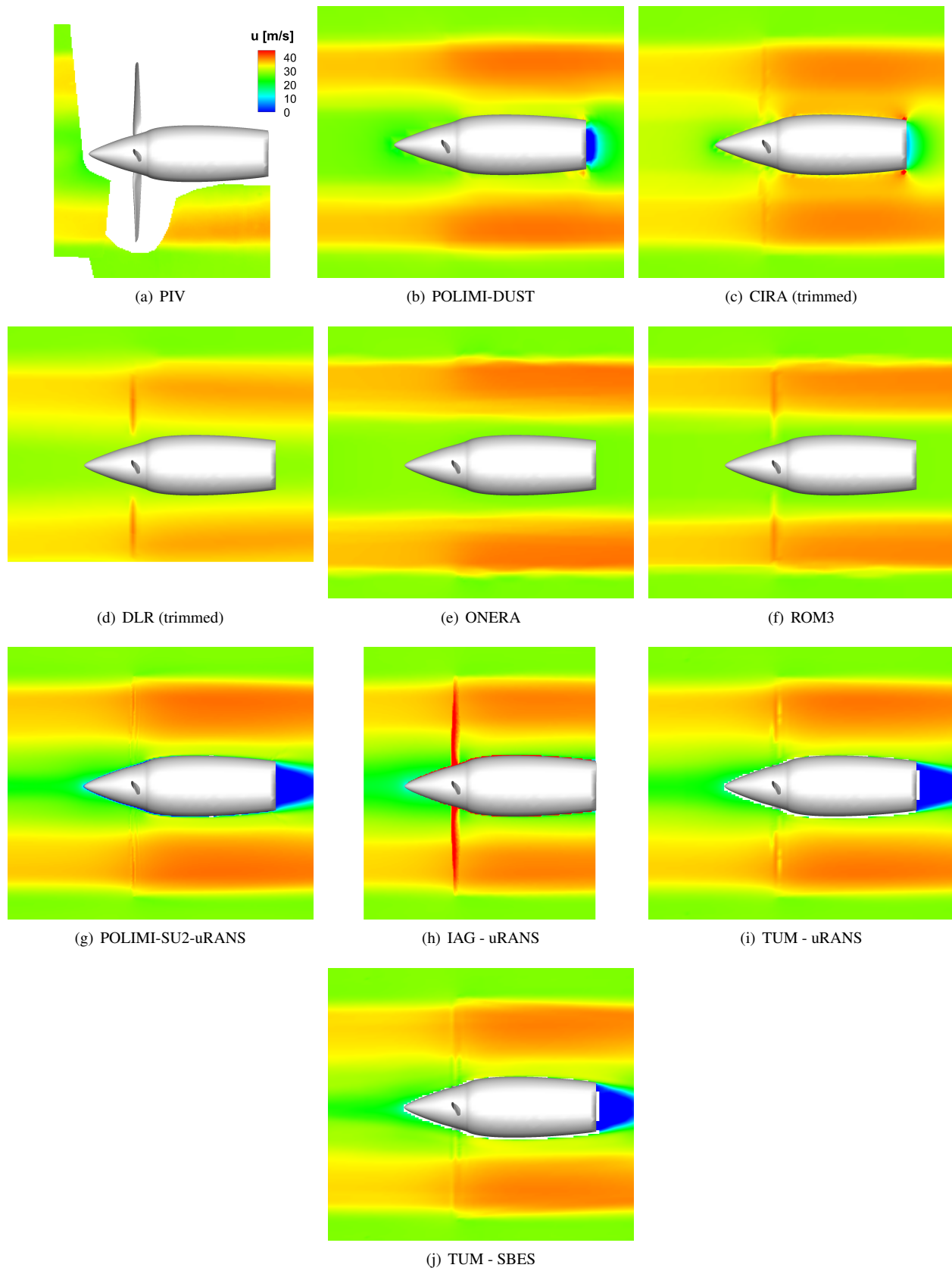**Figure 9.** **Contours of the averaged axial velocity component** (u) **for the tandem co-axial configuration CRF 2 (TP),** $L_x/R = 5$ **and** $L_y/R = 0$ **in cruise condition, rear propeller area.**
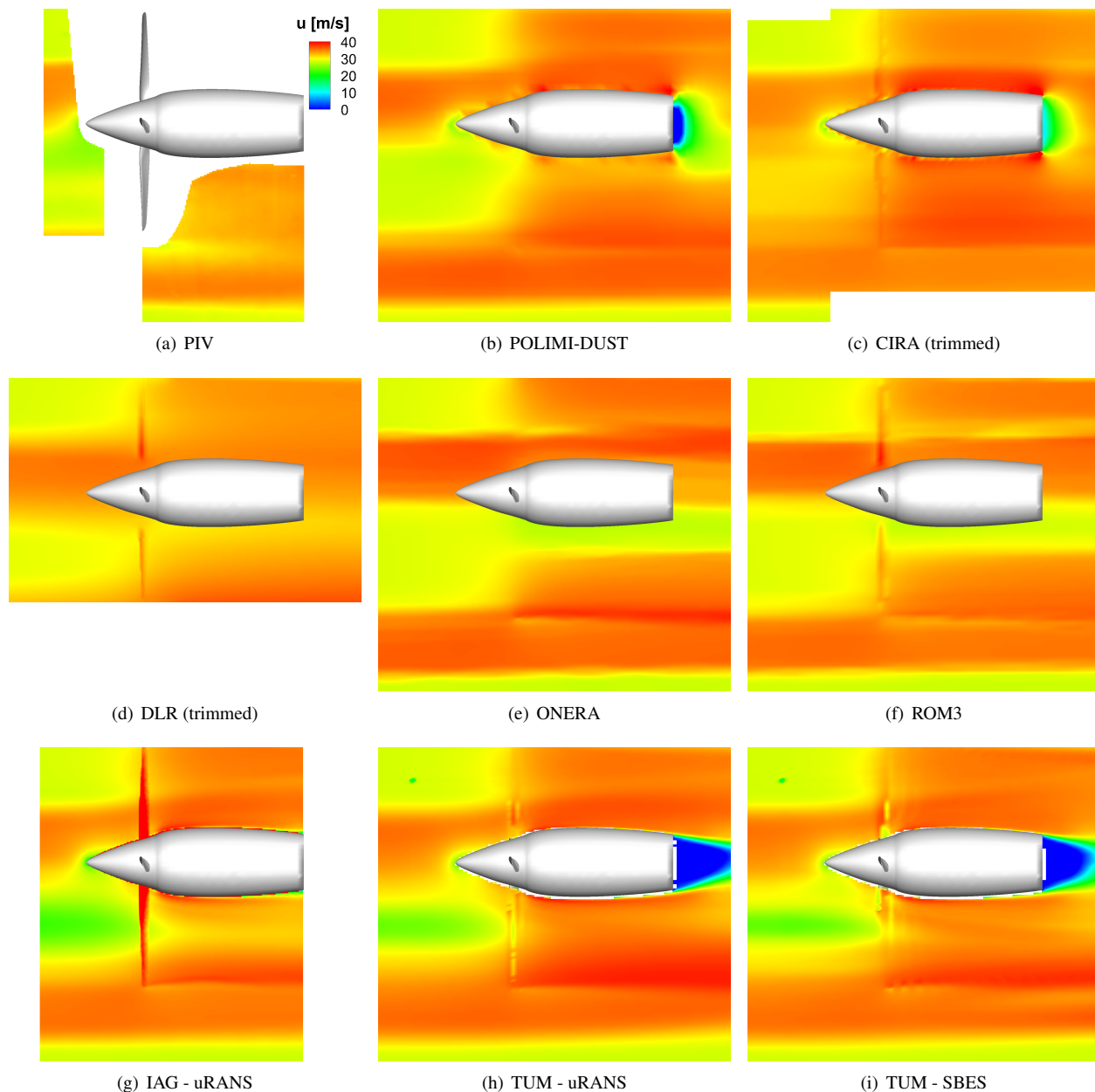
Figure 10. Contours of the averaged axial velocity component (u) for the tandem configuration CRF 4 (TP), $L_x/R = 5$ and $L_y/R = 1$, in cruise condition, rear propeller area.

classical dipole behaviour (see Fig. 13(a)). In the present test case, the high-fidelity CFD approach provides almost the same output of the mid-fidelity tools used by the partners, except the IAG approach that differently shows a symmetric circular behaviour of the SPL around the single propeller in cruise.

For the tandem co-axial configuration in cruise (CRF2), acoustics calculations based on uRANS high-fidelity simulations by POLIMI-SU2 shows again a dipole behaviour for the overall SPL that is not symmetrical considering the front and rear set of microphones, i.e $\theta = 90° - 270°$ direction (see Fig. 13(b)). This behaviour is reproduced by POLIMI-DUST, while mid-fidelity approaches by ROM3 as well as the

trimmed simulations by DLR and CIRA show a quite symmetrical dipole behaviour of the SPL. This latter feature is also evident in TUM's sound predictions based on uRANS blade loading. On the other hand, high-fidelity simulations based calculations from IAG and TUM-SBES shows a symmetrical circular behaviour characterised by higher values of the SPL upstream the front propeller and downstream the rear one. Since the SBES simulation much better conserves the axial evolution of the tip vortices, their break up and impingement on the blades of the rear propeller causes additional unsteady loads that are not present in TUM's uRANS prediction. The enhanced SPL along the axis is in agreement with the calculations based on mid-fidelity approach used by ONERA.
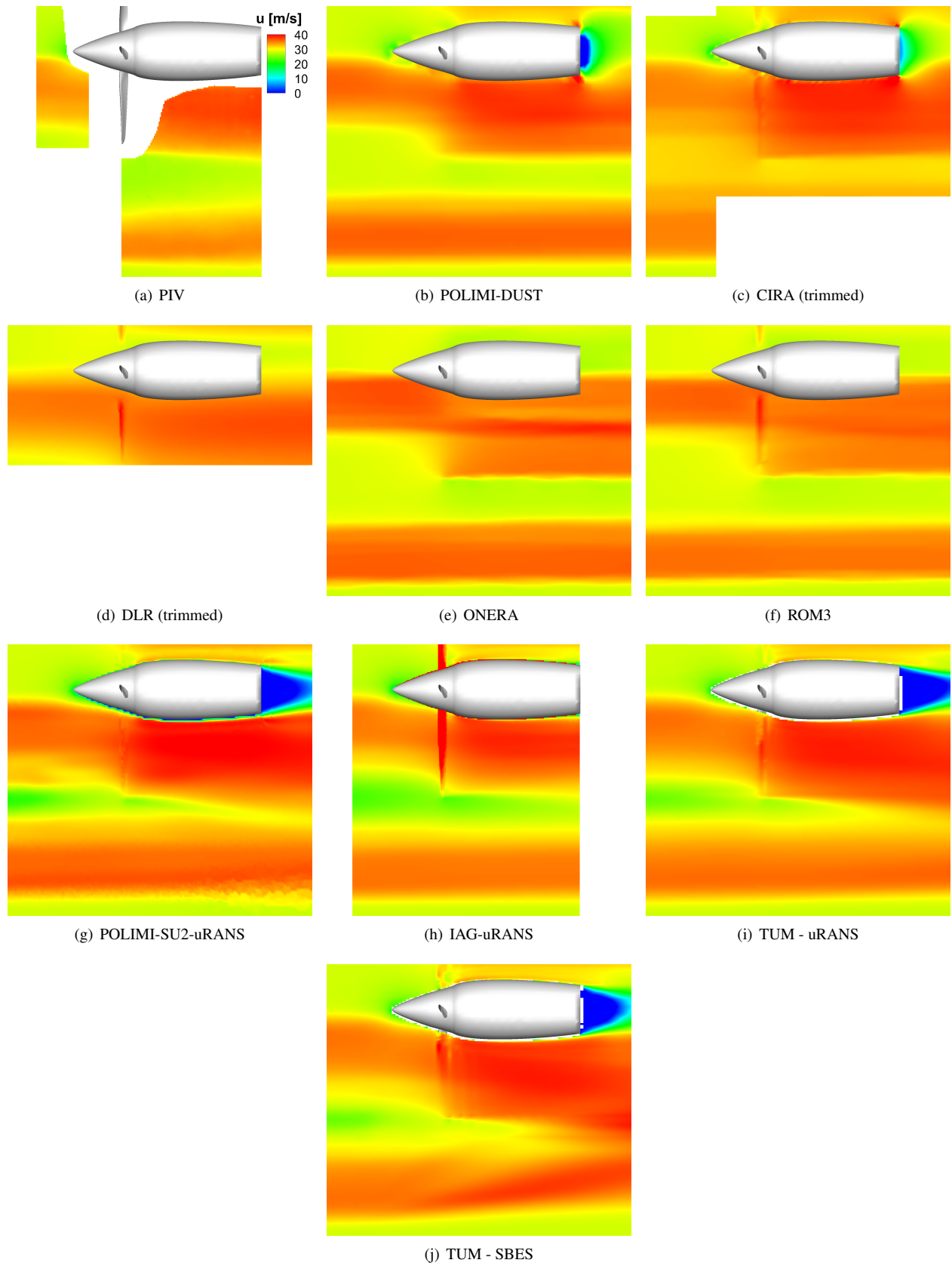
(a) PIV

(b) POLIMI-DUST

(c) CIRA (trimmed)

(d) DLR (trimmed)

(e) ONERA

(f) ROM3

(g) POLIMI-SU2-uRANS

(h) IAG-uRANS

(i) TUM - uRANS

(j) TUM - SBES

Figure 11. Contours of the averaged axial velocity component (u) for the tandem configuration CRF 3 (TP), $L_x/R = 5$ and $L_y/R = 1$, in cruise condition, rear propeller area.
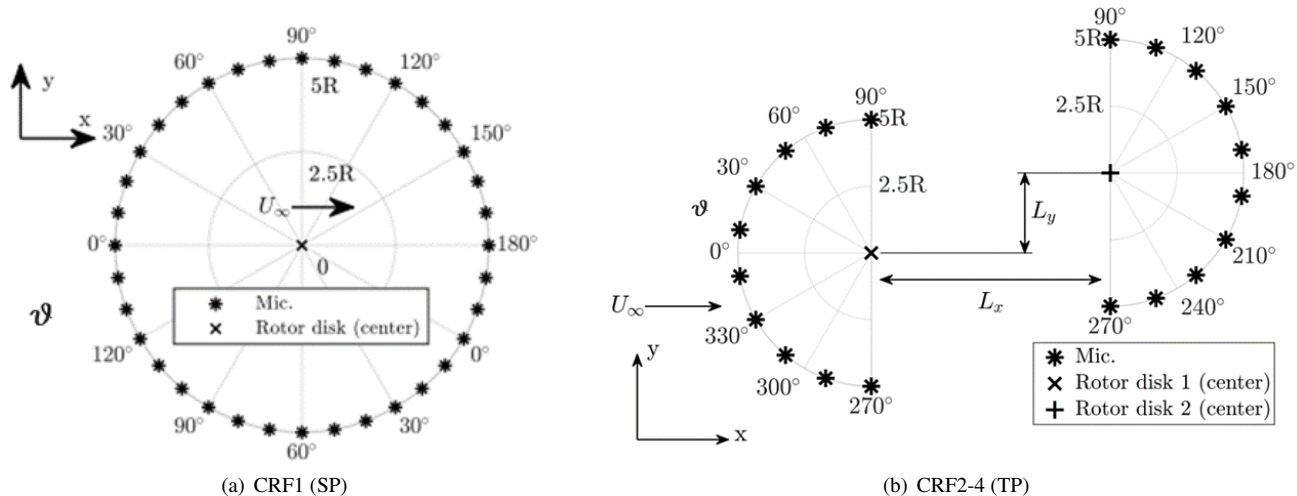
(a) CRF1 (SP)

(b) CRF2-4 (TP)

Figure 12. Position of virtual microphones for the cruise flight conditions.

(a) CRF1 (SP)

(b) CRF2 (TP), $L_x/R = 5$ and $L_y/R = 0$

(c) CRF3 (TP), $L_x/R = 5$ and $L_y/R = 0.5$

(d) CRF4 (TP), $L_x/R = 5$ and $L_y/R = 1$
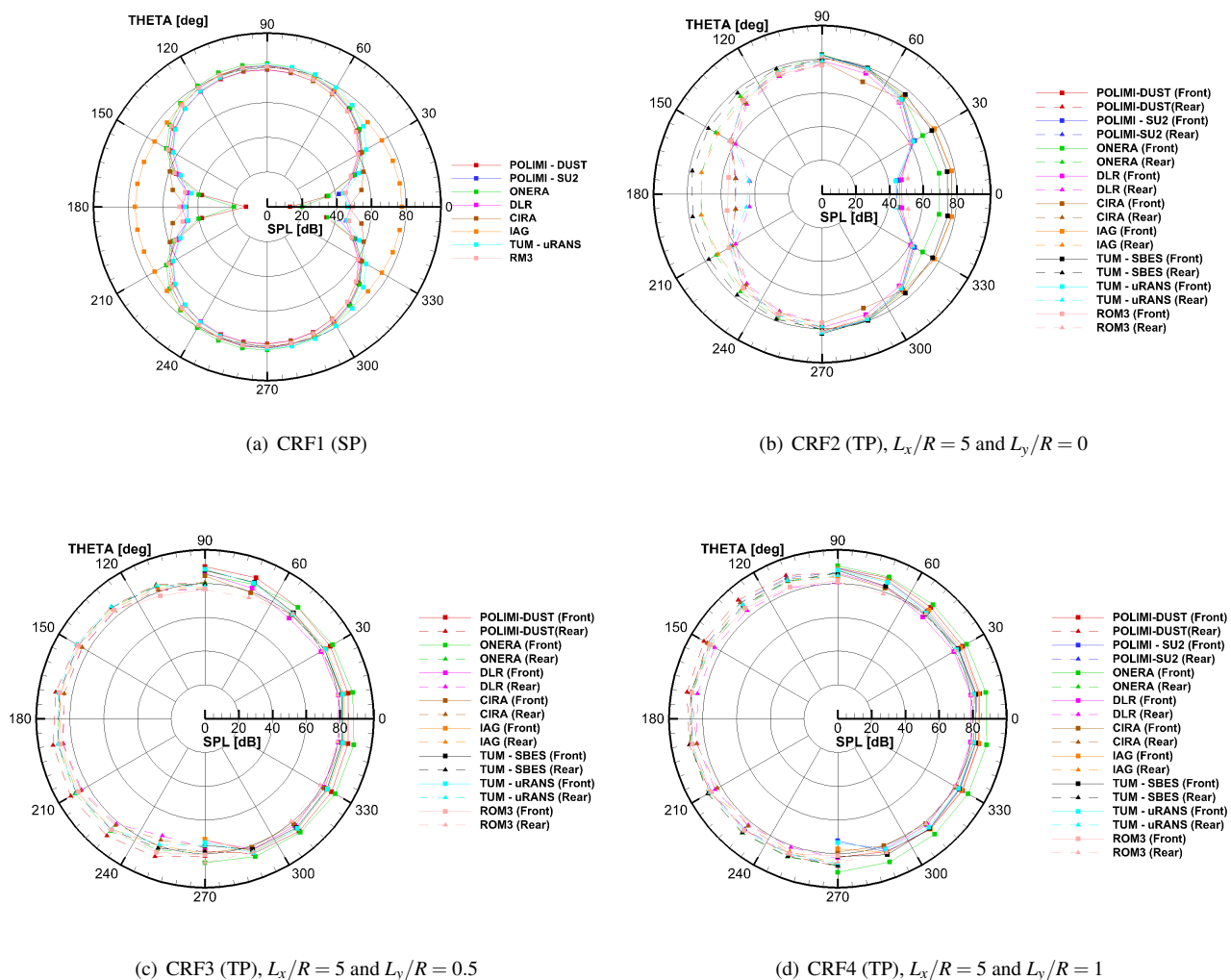
Figure 13. Overall Sound Pressure Level (SPL) for the configurations CRF 1-4 in cruise condition.

For the tandem configurations characterised by a partial overlap of the propellers disks in cruise, i.e. $L_y/R = 0.5$ and $L_y/R = 1$, the overall SPL calculated by both mid-fidelity and high-fidelity simulations used by the partners are in quite good agreement (see Figs. 13(c) and 13(d)). Indeed, all the approaches provide an almost symmetrical polar behaviour of the SPL for the front and rear propeller characterised by values of the SPL that are increased when the lateral overlap of the rotor disks is reduced. The increased noise level for the increasing staggered configurations is in accordance to the thrust spectral analysis of the rear propeller measured during the experimental campaign (Ref. 6).

Hover Flight Conditions

Aerodynamic Performance

As done for the test cases in cruise, a first analysis of the numerical solvers performance for the hover condition is provided by comparing the averaged thrust C_T and power coefficients C_T of the single propeller (HOV 1) calculated with the different numerical approaches with respect to experimental data, see Tab. 3.

	C_T	C_P
Experimental	0.1508	0.0713
POLIMI - DUST	0.1203	0.0502
POLIMI - SU2 (RANS RRF)	0.1440	0.0640
CIRA (trimmed)	0.1508	0.0086
DLR (trimmed)	0.1497	0.0097
ROM3	0.1168	0.0061

Table 3. Thrust and Power coefficients evaluated for the single propeller in hover flight condition HOV 1 (SP) by the different computational methods.

A good agreement was found for the aerodynamic loads evaluated by POLIMI high-fidelity CFD solver, particularly for C_T (below 1%), while a slightly larger relative difference with respect to experimental value was found for C_P. DUST mid-fidelity approach underestimates both the thrust and power coefficients, respectively by almost 20% and 30% with respect to experiments. Thrust coefficient evaluation is almost in accordance with the not trimmed solutions by ROM3. Mid-fidelity solutions by DLR and CIRA are trimmed on thrust coefficient value, while a conspicuous underestimation of the C_P experimental value is found due to their pure potential approaches, analogously to what found for the same reason by ROM3 simulations.

Simulations results for the tandem configurations (HOV 2-4) obtained by the different numerical approaches are compared to experimental data in Fig. 14. In particular, to better evaluate the performance of the solvers to capture the aerodynamic performance losses of the rear propeller due to the interaction of the front propeller slipstream, the ratio of the thrust and power coefficients evaluated for the rear propeller with respect to single propeller (HOV 1) is shown. For $L_y/R < 2$

the rotor disk of the rear propeller is partially overlapped to the front propeller one.
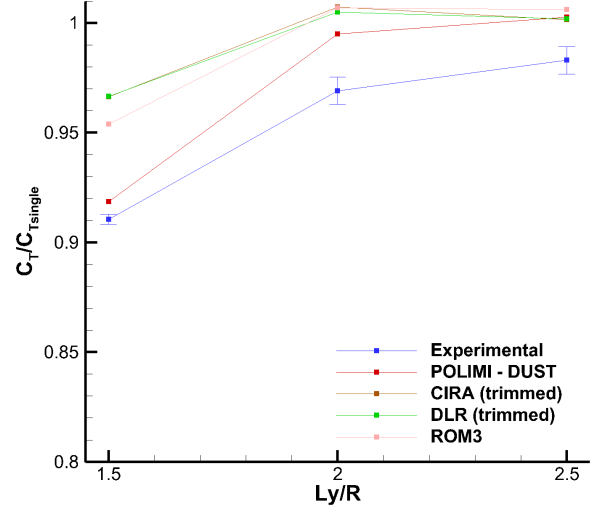
(a)
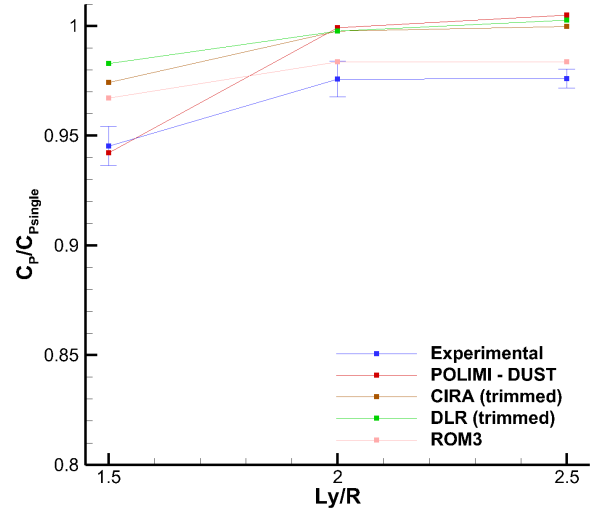
(b)

Figure 14. Thrust and Power coefficients evaluated for the rear propeller in tandem HOV 2-4 (TP) with respect to single propeller HOV 1 (SP) in hover flight condition by the different computational methods.

Looking at the experimental aerodynamic performance data, rear propeller thrust and power slightly decreases up to $L_y/R < 2$, while for lower lateral distance characterised by propeller disk overlapping, a decrease up to almost 10% and 5% respectively of the single propeller C_T and C_P was observed. This effect is related to the fact that the reference propeller disk is invested by front propeller slipstream in the overlapped configuration ($L_y/R = 1.5$).
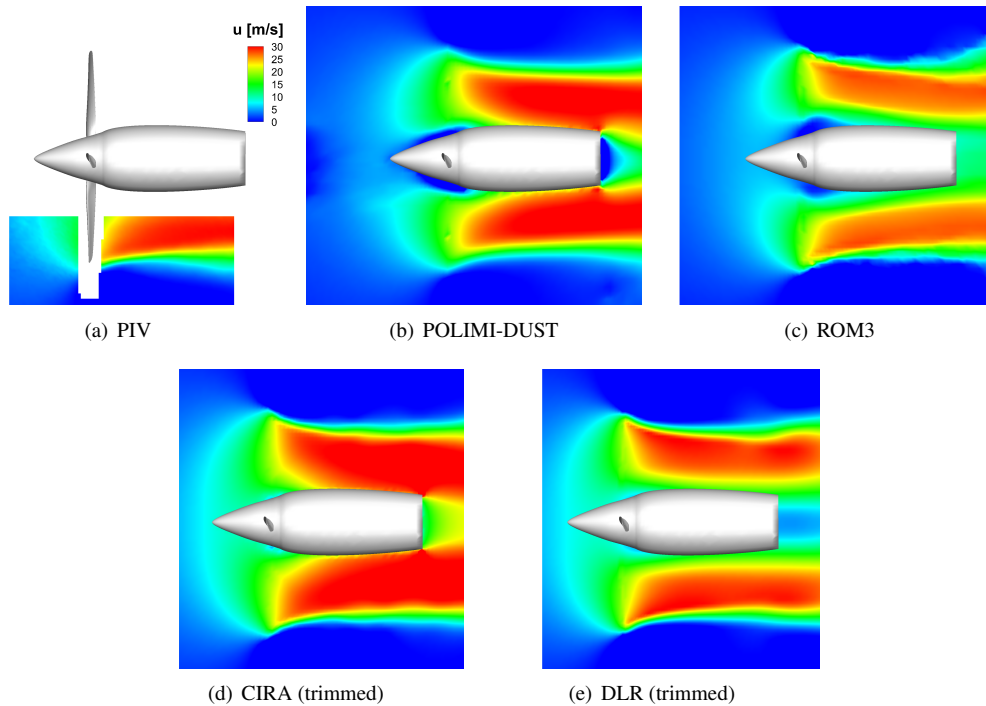
14

Figure 15. Contours of the averaged axial velocity component (u) for the single propeller configuration HOV 1 (SP) in hover condition, rear propeller area.
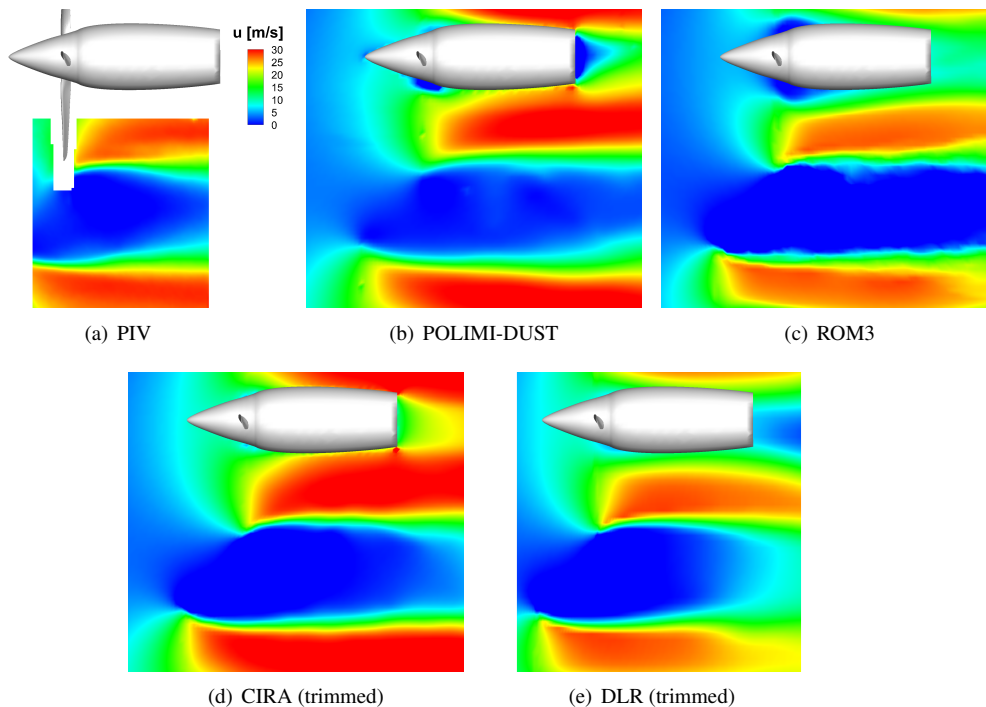

Figure 16. Contours of the averaged axial velocity component (u) for the tandem propeller configuration HOV 2 (TP) in hover condition, $L_x/R = 0.5$ and $L_y/R = 2.5$, rear propeller area.

The trend of thrust coefficient ratio curve is captured by numerical simulations. In particular, a slight mismatch of the performance losses with respect to experiments was found for the higher lateral distances $L_y/R = 2$ and $L_y/R = 2.5$ considering all the solutions. For the configuration with partial overlapped propellers disks $L_y/R = 1.5$ characterised by the highest aerodynamic interactional effects, DUST solution captures quite well the experimental performance losses of the
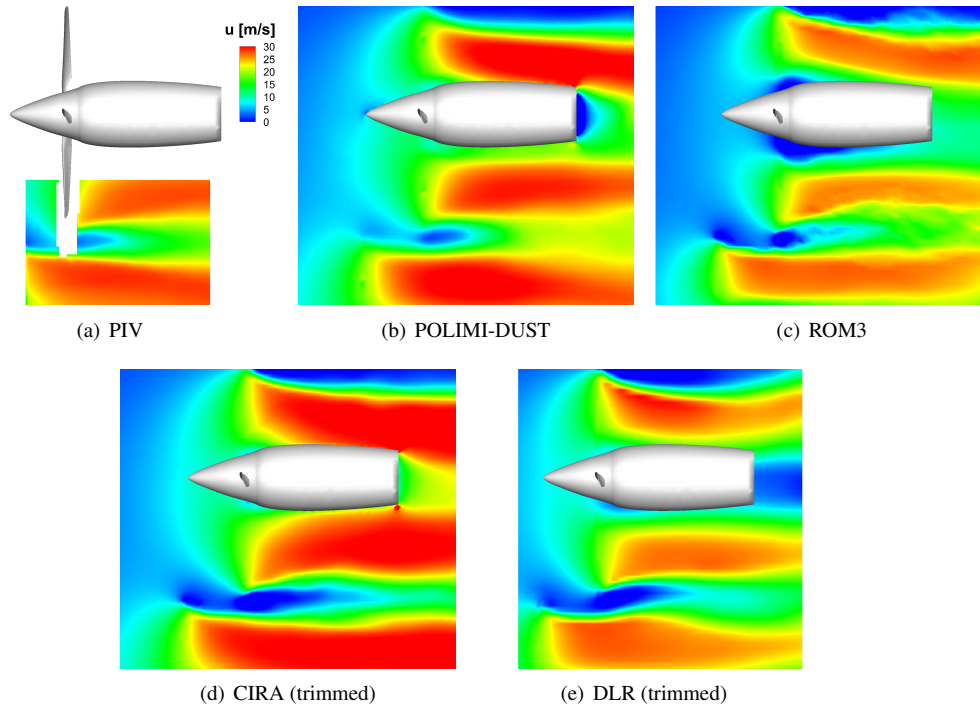
Figure 17. Contours of the averaged axial velocity component (u) for the tandem propeller configuration HOV 3 (TP) in hover condition, $L_x/R = 0.5$ and $L_y/R = 2$, rear propeller area.
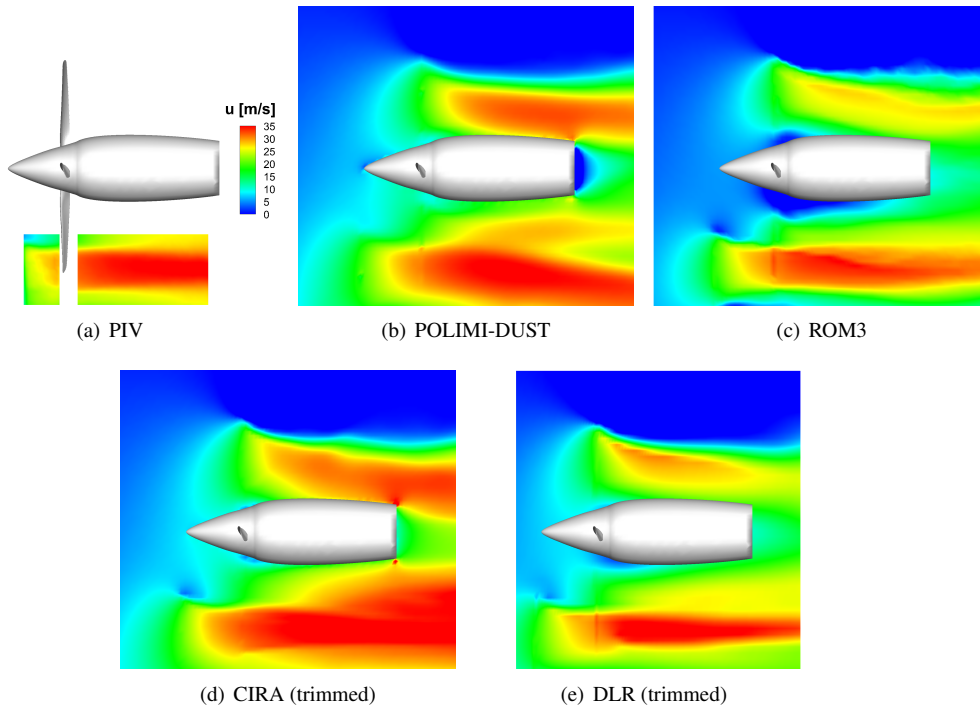

Figure 18. Contours of the averaged axial velocity component (u) for the tandem propeller configuration HOV4 (TP) in hover condition, $L_x/R = 0.5$ and $L_y/R = 1.5$, rear propeller area.

rear propeller for both the aerodynamic coefficients considered, while higher discrepancies in the order of 5% and 3% respectively of the experimental C_T and C_P was observed for the trimmed solutions by CIRA and DLR. ROM3 solution, not trimmed, resembles results similar to these two latter approaches concerning both the thrust and power loss. High-fidelity numerical solutions were not available for these tandem test cases at the moment of paper submission but are

scheduled before the end of the GARTEUR Action Group.

Aerodynamic solutions analysis is completed by the comparison of the averaged flow fields evaluated by the different numerical solvers with respect to PIV data. In particular, Figs. 15-18 show the comparison of the contours of the averaged axial velocity component (u) for the single propeller configuration HOV 1 and the tandem configurations HOV 2-4 around the rear propeller region.

For the single propeller configuration, the flow field comparison shows a quite good agreement between the numerical solutions and PIV survey. Indeed, the accelerated propeller slipstream is quite well captured by numerical simulations (see Fig. 15), with a slight underestimation provided by ROM3 solution. For the tandem configuration with $L_y/R = 2.5$ the flow field measured by PIV shows weak interactional effects on the slipstreams of the two propellers (see Fig. 16). The same considerations made for the single propeller configurations can be done for this test condition as the flow field for the rear propeller resembles the single propeller one.

For the tandem configuration with $L_y/R = 2$, the interaction between the propeller flows is more pronounced as shown by PIV data, particularly at the boundary of the rear propeller slipstream (see Fig. 17). This interacting flow region between the two propellers is quite well captured by DUST and ROM3 solutions. Similarly to what found for the previous test case, DLR and ROM3 solutions shows a slight underestimation of the velocity in the propellers slipstreams with respect to experiments.

For the tandem configuration with $L_y/R = 1.5$, as the propellers disks overlap for a certain portion, the interaction of the slipstreams results in a highly accelerated flow (see Fig. 18). The magnitude of the axial velocity in this region is quite well captured by all the numerical solutions, with a slight underestimation observed from DLR and ROM3 solution. Moreover, DUST solution shows a downward deflection of the rear propeller wake.

Aeroacoustics

Aeroacoustics evaluation was compared in terms of the overall SPL in polar diagram evaluated at the microphones positions shown in Fig. 5.

For the single propeller configuration in hover (HOV 1), the experimental overall SPL does not show a specific directivity. On the other hand, numerical calculations show a dipole-like behaviour on the SPL. Thus, a certain mismatch is found with respect to the experiments just in front and in the wake of the propeller, respectively at $\theta = 0°$ and $\theta = 180°$. This latter feature is particularly evident from the calculation based of POLIMI-SU2 high-fidelity simulation. Noise level evaluated by mid-fidelity approaches by the partners tend to be more similar to experimental behaviour, with a better matching observed for DLR and ROM3 solutions.

For the tandem configuration with $L_y/R = 2.5$, noise level increases with respect to the single propeller configuration and shows a not symmetrical behaviour that resembles the propellers configuration. Numerical evaluation shows a good

agreement with experiments except in region in front of the propellers where all numerical approaches show an underestimation of the SPL. On the other hand, discrepancies with experimental values observed for POLIMI, CIRA and ROM3 are quite lower at sides and downstream the propellers, while DLR calculation shows larger discrepancies along all the directions.

For the tandem configuration with $L_y/R = 2$, the experimental overall SPL shows a slight increase with respect to the previous configuration due to a limited increase of aerodynamic interaction occurring by decreasing the lateral distance between propellers. In the present case, the agreement between numerical calculation and experiments is quite higher as discrepancies in the order of few dB are found for all numerical approaches.

For the tandem configuration with $L_y/R = 1.5$, the interaction of the slipstreams related to propellers disks partial overlap provides an increase of the noise level of about 10 dB along all the directions, as can be observed from experiments. In this case, the numerical calculations based on mid-fidelity simulations are capable to appreciate this increase of SPL. Generally the agreement with experimental values is quite good with observed discrepancies in the order of few dBs.

CONCLUSIONS

In the present paper, experimental and numerical activities achieved in the GARTEUR AG26 on the POLIMI dual propeller set up. Aerodynamic and aeroacoustic results were described and compared. In particular, different flight configurations from cruise to hover were investigated as well as conditions characterised by a high degree of aerodynamic interaction due to propellers disks overlap. Comparisons of code-to-code and the code-to-test results enabled to evaluate the capabilities of mid-fidelity to high-fidelity approaches for the calculation of both aerodynamic performance and acoustics of a challenging test configuration. Both aerodynamic and aeroacoustic simulations indicate that measurements results in terms of rotor performance, flow fields and acoustic signatures for most cases were reproducible and that comparison of the simulations and the tests give satisfactory agreements by all computational methods, regardless of their fidelity level. In particular, the numerical predictions reproduced the correct trends with respect to changes in the lateral distance, emphasizing their usefulness for design studies of novel eVTOL aircraft.
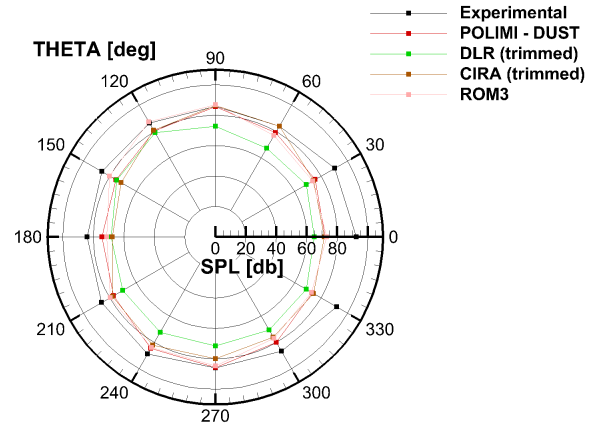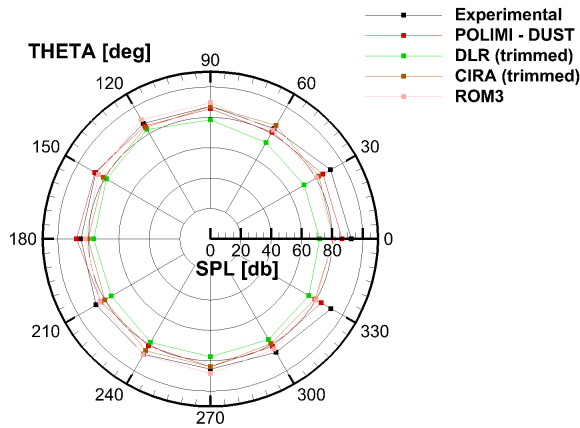
ACKNOWLEDGEMENTS

REFERENCES

1. Thai, A. D., De Paola, E., Di Marco, A., Stoica, L. G., Camussi, R., Tron, R., and Grace, S. M., "Experimental and Computational Aeroacoustic Investigation
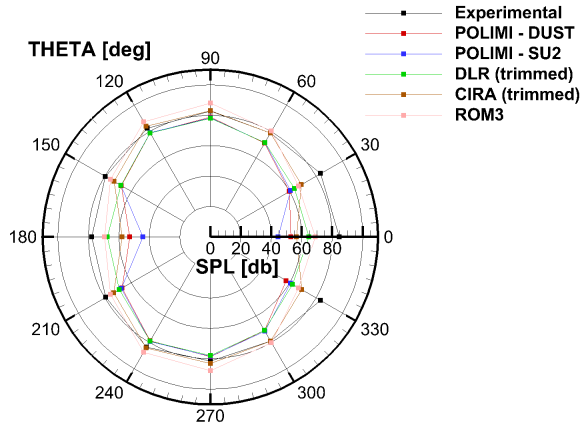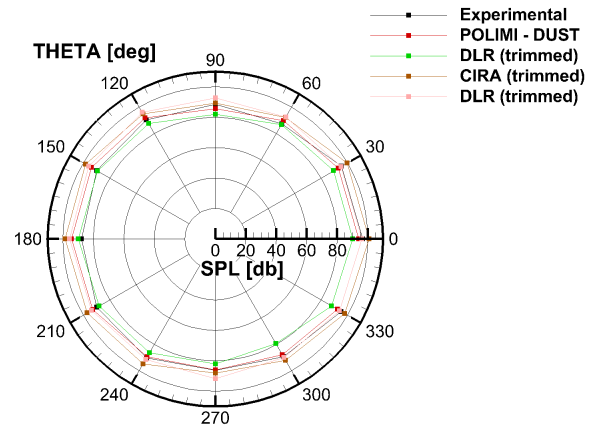
(a) HOV1 (SP)

(b) HOV2 (TP), $L_x/R = 0.5$ and $L_y/R = 2.5$

(c) HOV3 (TP), $L_x/R = 0.5$ and $L_y/R = 2$

(d) HOV4 (TP), $L_x/R = 0.5$ and $L_y/R = 1.5$

Figure 19. Overall Sound Pressure Level (SPL) for the propeller configurations HOV 1-4 in hover condition.

of Small Rotor Interactions in Hover," *Applied Sciences*, Vol. 11, (21), 2021.

2. Jia, Z., and Lee, S., "Acoustic Analysis of a Quadrotor eVTOL Design via High-Fidelity Simulations," 25th AIAA/CEAS Aeroacoustics Conference, 2019.

3. Poggi, C., Bernardini, G., Gennaretti, M., and Camussi, R., "Scalability of Mach Number Effects on Noise Emitted by Side-by-Side Propellers," *Applied Sciences*, Vol. 12, (19), 2022.

4. Yin, J., De Gregorio, F., Rossignol, K.-S., Rottmann, L., Ceglia, G., Reboul, G., Barakos, G., Qiao, G., Muth, M., Kessler, M., Visingardi, A., Barbarino, M., Petrosino,

F., Zanotti, A., Oberti, N., Galimberti, L., Bernardini, G., Poggi, C., Abergo, L., Caccia, F., Guardone, A., Testa, C., and Zaghi, S., "ACOUSTIC AND AERODYNAMIC EVALUATION OF DLR SMALL-SCALE ROTOR CONFIGURATIONS WITHIN GARTEUR AG26," 49th European Rotorcraft Forum, 2023.

5. Nargi, R. E., Candeloro, P., De Gregorio, F., Ceglia, G., and Pagliaroli, T., "Fluid-Dynamic and Aeroacoustic Characterization of Side-by-Side Rotor Interaction," *Aerospace*, Vol. 10, (10), 2023, pp. 851.

6. Zanotti, A., and Algarotti, D., "Aerodynamic interaction between tandem overlapping propellers in eVTOL airplane mode flight condition," *Aerospace Sci-*

ence and Technology, Vol. 124, 2022, pp. 107518. DOI: https://doi.org/10.1016/j.ast.2022.107518.

7. Zanotti, A., Velo, A., Pepe, C., Savino, A., Grassi, D., and Riccobene, L., "Aerodynamic interaction between tandem propellers in eV-TOL transition flight configurations," *Aerospace Science and Technology*, 2024, pp. 109017. DOI: https://doi.org/10.1016/j.ast.2024.109017.

8. Droandi, G., Syal, M., and Bower, G., "Analysis of the Interactional Aerodynamics of the Vahana eVTOL Using a Medium Fidelity Open Source Tool," Proceedings of the VFS Aeromechanics for Advanced Vertical Flight Technical Meeting, January 21-23 2020.

9. Johnson, W., Silva, C., and Solis, E., "Concept Vehicles for VTOL Air Taxi Operations," Proceedings of the AHS Technical Conference on Aeromechanics Design for Transformative Vertical Flight, January 16-19 2018.

10. Silva, C., Johnson, W., Solis, E., Patterson, M. D., and Antcliff, K. R., "VTOL Urban Air Mobility Concept Vehicles for Technology Development," Proceedings of the AIAA Aviation Technology, Integration, and Operations Conference, June 25-29 2018.

11. Droandi, G., Syal, M., and Bower, G., "Tiltwing Multi-Rotor Aerodynamic Modeling in Hover, Transition and Cruise Flight Conditions," Proceedings of the 74th Annual Forum, May 2018.

12. Tugnoli, M., Montagnani, D., Syal, M., Droandi, G., and Zanotti, A., "Mid-fidelity approach to aerodynamic simulations of unconventional VTOL aircraft configurations," *Aerospace Science and Technology*, Vol. 115, 2021, pp. 106804. DOI: https://doi.org/10.1016/j.ast.2021.106804.

13. Economon, T. D., Palacios, F., Copeland, S. R., Lukaczyk, T. W., and Alonso, J. J., "SU2: An open-source suite for multiphysics simulation and design," *Aiaa Journal*, Vol. 54, (3), 2016, pp. 828–846.

14. Economon, T. D., Palacios, F., and Alonso, J. J., *A Viscous Continuous Adjoint Approach for the Design of Rotating Engineering Applications*, American Institute of Aeronautics and Astronautics, 2013. DOI: 10.2514/6.2013-2580.

15. Farrell, P. E., Piggott, M. D., Pain, C. C., Gorman, G. J., and Wilson, C. R., "Conservative interpolation between unstructured meshes via supermesh construction," *Computer methods in applied mechanics and engineering*, Vol. 198, (33-36), 2009, pp. 2632–2642. DOI: 10.1016/j.cma.2009.03.004.

16. Rinaldi, E., Colonna, P., and Pecnik, R., "Flux-conserving treatment of non-conformal interfaces for finite-volume discretization of conservation laws," *Computers & Fluids*, Vol. 120, 2015, pp. 126–139. DOI: https://doi.org/10.1016/j.compfluid.2015.07.017.

17. Jameson, A., Schmidt, W., and Turkel, E., "Numerical solution of the Euler equations by finite volume methods using Runge Kutta time stepping schemes," 14th fluid and plasma dynamics conference, 1981. DOI: 10.2514/6.1981-1259.

18. Spalart, P., and Allmaras, S., "A one-equation turbulence model for aerodynamic flows," Proceedings of the 30th Aerospace Sciences Meeting and Exhibit, 1994. DOI: 10.2514/6.1992-439.

19. Cakmakcioglu, S. C., Bas, O., Mura, R., and Kaynak, U., "A Revised One-Equation Transitional Model for External Aerodynamics," Proceedings of the AIAA AVIATION 2020 FORUM, 15–19 June 2020. DOI: 10.2514/6.2020-2706.

20. Williams, J. F., and Hawkings, D. L., "Sound generation by turbulence and surfaces in arbitrary motion," *Philosophical Transactions for the Royal Society of London. Series A, Mathematical and Physical Sciences*, 1969, pp. 321–342.

21. Galimberti, L., Morelli, M., Guardone, A., and Zhou, B. Y., "Propeller Noise Prediction Capabilities within SU2," Proceedings of the AIAA SCITECH 2023 Forum, 23–27 January 2023. DOI: 10.2514/6.2023-1548.

22. Ahmed, S., and Vidjaja, V., "Unsteady panel method calculation of pressure distribution on BO 105 model rotor blades," *Journal of the American Helicopter Society*, Vol. 43, (1), 1998, pp. 47–56.

23. Yin, J., and Ahmed, S., "Helicopter Main-Rotor/Tail-Rotor Interaction," *Journal of the American Helicopter Society*, Vol. 4, 2000, pp. 293–302.

24. Yin, J., van der Wall, B. G., and Wilke, G. A., "Rotor aerodynamic and noise under influence of elastic blade motion and different fuselage modeling," European Rotorcraft Forum, 2-5 September 2014, Southampton, 2014.

25. Boisard, R., "Numerical analysis of rotor/propeller aerodynamic interactions on a high-speed compound helicopter," *Journal of the American Helicopter Society*, Vol. 67, (1), 2022, pp. 1–15.

26. Mudry, M., *La théorie des nappes tourbillonnaires et ses applications à l'aérodynamique instationnaire*, Ph.D. thesis, University of Paris VI, 1982.

27. Cambier, L., Heib, S., and Plot, S., "The Onera elsA CFD software: input from research and feedback from industry," *Mechanics & Industry*, Vol. 14, (3), 2013, pp. 159–174.

28. Prieur, J., and Rahier, G., "Comparison of Ffowcs Williams-Hawkings and Kirchhoff rotor noise calculations," 4th AIAA/CEAS aeroacoustics conference, 1998.

29. Rahier, G., and Prieur, J., "An efficient Kirchhoff integration method for rotor noise prediction starting indifferently from subsonically or supersonically rotating meshes," Paper 1997-48, AHS, Annual Forum, 53 rd, Virginia Beach, VA, Apr. 29-May 1, 1997, ONERA, TP, 1997.

30. Raddatz, J., and Fassbender, J. K., "Block structured navier-stokes solver flower," MEGAFLOW-Numerical Flow Simulation for Aircraft Design: Results of the second phase of the German CFD initiative MEGAFLOW, presented during its closing symposium at DLR, Braunschweig, Germany, December 10 and 11, 2002, 2005.

31. Kowarsch, U., Oehrle, C., Hollands, M., Keßler, M., and Krämer, E., "Computation of helicopter phenomena using a higher order method," High Performance Computing in Science and Engineering '13: Transactions of the High Performance Computing Center, Stuttgart (HLRS) 2013, 2013.

32. Schuff, M., Kranzinger, P., Keßler, M., and Krämer, E., "Advanced CFD-CSD coupling: Generalized, high performant, radial basis function based volume mesh deformation algorithm for structured, unstructured and overlapping meshes," European Rotorcraft Forum, 2-5 September 2014, Southampton, 2014.

33. Kessler, M., and Wagner, S., "Source-time dominant aeroacoustics," *Computers Fluids*, Vol. 33, (5), 2004, pp. 791–800.

34. Menter, F. R., Kuntz, M., Langtry, R., *et al.*, "Ten years of industrial experience with the SST turbulence model," *Turbulence, heat and mass transfer*, Vol. 4, (1), 2003, pp. 625–632.

35. Borges, R., Carmona, M., Costa, B., and Don, W. S., "An improved weighted essentially non-oscillatory scheme for hyperbolic conservation laws," *Journal of Computational Physics*, Vol. 227, (6), 2008, pp. 3191–3211.

36. Visingardi, A., D'Alascio, A., Pagano, A., and Renzoni, P., "Validation of CIRA's Rotorcraft Aerodynamic Modelling System with DNW experimental data," , 1996.

37. Morino, L., and Kuot, C.-C., "Subsonic potential aerodynamics for complex configurations: a general theory," *AIAA Journal*, Vol. 12, (2), 1974, pp. 191–197.

38. Casalino, D., "An advanced time approach for acoustic analogy predictions," *Journal of Sound and Vibration*, Vol. 261, (4), 2003, pp. 583–612.

39. Casalino, D., Barbarino, M., and Visingardi, A., "Simulation of helicopter community noise in complex urban geometry," *AIAA journal*, Vol. 49, (8), 2011, pp. 1614–1624.

40. Barbarino, M., Petrosino, F., and Visingardi, A., "A high-fidelity aeroacoustic simulation of a VTOL aircraft in an urban air mobility scenario," *Aerospace Science and Technology*, Vol. 125, SI: DICUAM 2021, 2022, pp. 107104.

41. Scheit, C., Karic, B., and Becker, S., "Effect of blade wrap angle on efficiency and noise of small radial fan impellers—A computational and experimental study," *Journal of Sound and Vibration*, Vol. 331, (5), 2012, pp. 996–1010.

42. Gennaretti, M., Bernardini, G., Serafini, J., and Romani, G., "Rotorcraft comprehensive code assessment for blade–vortex interaction conditions," *Aerospace Science and Technology*, Vol. 80, 2018, pp. 232–246.

43. Gennaretti, M., Colella, M. M., and Bernardini, G., "Prediction of tiltrotor vibratory loads with inclusion of wing-proprotor aerodynamic interaction," *Journal of Aircraft*, Vol. 47, (1), 2010, pp. 71–79.

44. Gennaretti, M., and Bernardini, G., "Novel boundary integral formulation for blade-vortex interaction aerodynamics of helicopter rotors," *AIAA journal*, Vol. 45, (6), 2007, pp. 1169–1176.

45. Farassat, F., "Derivation of Formulations 1 and 1A of Farassat," Technical report, 2007.